Conformational dynamics of the inner pore helix of voltage-gated potassium channels

Seungho Choe[1] and Michael Grabe[1,2,a)]
[1]*Department of Biological Sciences, University of Pittsburgh, Pittsburgh, Pennsylvania 15260, USA*
[2]*Department of Computational Biology, School of Medicine, University of Pittsburgh, Pittsburgh, Pennsylvania 15260, USA*

(Received 23 December 2008; accepted 24 April 2009; published online 4 June 2009)

Voltage-gated potassium (Kv) channels control the electrical excitability of neurons and muscles. Despite this key role, how these channels open and close or gate is not fully understood. Gating is usually attributed to the bending and straightening of pore-lining helices at glycine and proline residues. In this work we focused on the role of proline in the Pro-Val-Pro (PVP) motif of the inner S6 helix in the Kv1.2 channel. We started by developing a simple hinged-rod model to fully explore the configurational space of bent helices and we related these configurations to the degree of pore opening. We then carried out fully atomistic simulations of the S6 helices and compared these simulations to the hinged-rod model. Both methods suggest that Kv1 channels are not tightly closed when the inner helices are straight, unlike what is seen in the non-PVP containing channels KcsA and KirBac. These results invite the possibility that the S6 helices may be kinked when Kv1 channels are closed. Our simulations indicate that the wild-type helix adopts multiple spatially distinct configurations, which is consistent with its role in adopting a closed state and an open state. The two most dominant configurational basins correspond to a 6 Å movement of the helix tail accompanied by the PVP region undergoing a local α-helix to 3_{10}-helix transition. We explored how single point mutations affect the propensity of the S6 helix to adopt particular configurations. Interestingly, mutating the first proline, P405 (P473 in Shaker), to alanine completely removed the bistable nature of the S6 helix possibly explaining why this mutation compromises the channel. Next, we considered four other mutations in the area known to affect channel gating and we saw similarly dramatic changes to the helix's dynamics and range of motion. Our results suggest a possible mechanism of helix pore closure and they suggest differences in the closed state of glycine-only channels, like KcsA, and PVP containing channels. © *2009 American Institute of Physics*. [DOI: 10.1063/1.3138906]

I. INTRODUCTION

The presence of the plasma membrane makes it possible for cells to maintain a specialized intracellular environment compatible with cell survival and proper function. Consequently, communication with the external environment requires signals to be passed back and forth across this barrier, and this transfer must be tightly regulated to maintain cellular conditions. Ion channels are membrane proteins that play a central role in facilitating this communication. Channels span the membrane and they contain aqueous pore domains that selectively permit specific ions and molecules to move from one side of the membrane to the other. Controlling when and how these channels are open is critical to maintaining cellular homeostasis. Therefore, the final step in ion channel regulation is often the opening or closing of this pore domain, a process known as gating. Channels have evolved specific domains to interact with their environment by binding ligands or interacting with the electric field across the membrane. Changes in these domains are allosterically coupled to the central pore of the channel directly causing it to gate. For instance, voltage-gated ion channels are integral membrane proteins that contain voltage-sensing domains that respond to changes in membrane potential and transmit these changes to a pore domain that selectively passes potassium, sodium, or calcium,[1,2] while G-protein coupled inward rectifying potassium channels (GIRKs) open by binding G$\beta\gamma$ on the intracellular side of the membrane. X-ray crystallographic studies of the TM domains of ion channels provided considerable insights into the relationship between channel structure and function.[3–7] However, there are open questions concerning the configurational arrangements associated with the opening and closing of channel pore domains.

Extensive mutational and structural data implicate the pore-lining inner helix as a gate that adopts different conformations when potassium channels open and close. This segment is generally called the M2 helix in 2-transmembrane (TM) spanning channels or the S6 helix in 6-TM voltage-gated channels. Potassium channels are composed of four highly homologous subunits, and crystal structures often reveal fourfold symmetry along the pore axis. In the closed state of the *p*H sensitive KcsA channel, the pore-lining inner helices form an inverted "teepee." The helices cross at the apex of the teepee near the intracellular side of the membrane[7] and analysis of the crossing point reveals that the

a)Electronic mail: mdgrabe@pitt.edu.

channel subunits are too tightly packed to permit ions to enter the channel from the cytoplasm. By comparison, the structure of the calcium-activated MthK channel revealed that the inner helices are splayed apart creating a 12 Å wide unobstructed pathway for ions to move into the channel from the cytoplasm.[4] Closer comparison of the open-state MthK structure reveals that the inner helices adopt a strong kink at glycine, G83 (G99 in KcsA), which is highly conserved in both 2-TM and 6-TM potassium channels.[4] Recently, Alam and Jiang reported the high-resolution structure of the NaK channel in an open conformation.[8] A comparison of this open state with that of the previously determined closed state[9] revealed that major conformational changes occur in the inner helices at residue G87, the conserved G99 residue in KcsA. Further analysis supports the notion that gating is dominated by a hinge bending at the conserved glycine residue.

Functional studies confirm that the inner helices move during gating. Perozo *et al.*[10] used spin labeling and electron paramagnetic resonance spectroscopy to show that the inner helices of KcsA translate outward and rotate counterclockwise (as seen from extracellular side) as the channel opens, and single molecule studies arrive at similar conclusions.[11] Additionally, Clayton *et al.*[12] deduced that the diameter of the bundle crossing expands by 7 Å during gating by comparing changes in the crystal structure of the cyclic nucleotide binding domain in the presence and absence of ligand. Normal mode following demonstrated that the gating transition in KcsA involves a counterclockwise rotation (as viewed from the extracellular side) and unwinding of the M2 helices at the bundle crossing point, lateral movement away from the channel axis, and transformation of the central vestibule into a wide domain fully integrated with the intracellular solution.[13] Meanwhile, MD simulations of KirBac1.1 suggest that the conformational change associated with gating involves concerted and/or sequential hinge-bending motions about conserved glycines G134 (equivalent to G83 in MthK), G143, and G137 in the M2 helix.[14] Thus, both theoretical and experimental evidences show that the gating transition may not always be a simple bend of the inner helices at the conserved glycine G99/G83, but the transition may involve more complex conformational changes. However, the strong structural similarity between the open-state structure of NaK and MthK suggests that, at least in a subclass of ion channels, the gating mechanism of hinge bending at the conserved glycine may be well conserved.

Mutagenesis studies confirm that channel opening and closing depends critically on the chemistry of the residue at the hinge point. In 2-TM channels the conserved glycine is essential for channel function.[15,16] The structure of the voltage-gated potassium channel KvAP also exhibits a bend centered on the same glycine.[17] However, many voltage-gated Kv channels, including the Shaker channel, contain a Pro-Val-Pro (PVP) motif located seven residues closer to the C-terminus of S6, which has been shown to be critical for channel gating.[18,19] Both functional studies and crystallography support the notion that the inner helices of open Shaker channels bend at the PVP region.[3,19,20] Moreover, whereas substitution of P405 in S6 by alanine or glycine compromises channel gating, channel function can be rescued by reintroducing prolines at particular positions above or below the motif region, confirming the importance of prolines, but obscuring the exact role of the PVP motif in gating.[18]

It is not surprising that glycine and proline residues are present in the inner helices of K^+ channels since it has been well established that they play important roles in allowing α-helices to deviate from their ideal conformations (e.g., see Ref. 21 and references therein). Both residues increase helix flexibility and both are prevalent at kinks.[22–25] Glycine allows helix bending and kinking due to the small size of its side chain.[25] On the other hand, proline is a fairly rigid residue, given that it has one fixed dihedral angle. However, proline introduces helix flexibility by disrupting hydrogen bonding along the backbone: the carbonyl oxygen of the $(i-4)$th residue cannot form its usual hydrogen bond to the ith residue when that position is occupied by a proline. This leads to non-α-helical ϕ-ψ angles at the proline and the position directly preceding the proline.[26] This disruption of backbone hydrogen bonding and introduction of unusual dihedral angles often provides the basis for helix kinking.

But what exactly are these residues doing to allow the central pore to open and close? This question is difficult to answer due to the lack of structures in both open and closed states. The high conservation of the glycine hinge residue, G83 in MthK, suggests that the inner pore domains of channels adopt similar conformations when they are open and closed. Are all open pores structurally similar to MthK and all closed pores structurally similar to KcsA? The bend is centered on the PVP region in Kv1.2, so clearly PVP containing helices behave differently from only-glycine containing inner helices. However, it is not known if it is appropriate to classify inner helices into these two broad categories; however, from an engineering perspective, this hypothesis is extremely appealing. Just as a door that swings inward always has its hinges on the inside, is the placement of the PVP motif or glycine on the helix crucial to how the inner helix moves? The high conservation of these two residues suggests that placement is crucial and this opens the possibility that sequences of inner helices all have intrinsic properties that make them ideally suited for their role in channel gating. If this is true, then these properties will be independent of the particular three dimensional fold of the channel. Such helices will be ideally suited for use in a wide range of channel pores regardless of the channels exact physiological role or how it is gated by environmental factors. Importantly, the properties of these helices will persist in the absence of the channel, and they can be efficiently probed using molecular simulations.

In the present study we have taken two approaches to investigate the role that proline plays in the gating of the inner helices of the Kv1.2 channel. First, a simple hinged-rod model was constructed to understand how hinge placement along the helix influences the angles and degree to which the inner helices must bend in order to open the channel. We compared the first proline in the PVP motif in Kv1.2 with G99 in KcsA to highlight how this placement affects the desired mechanics of helix bending. Next, we used completely unbiased molecular dynamics (MD) simulations to

investigate the natural motions of the S6 inner helices. We identified five mutations at or near the PVP motif and we simulated their influence on the natural motions of the helices. We relate the results of the MD simulations to the hinged-rod model to suggest that the inner helices have intrinsic properties that make them ideally suited to open and close channels.

II. MATERIALS AND METHODS

A. Hinged-rod model

We constructed a hinged-rod model to fully explore conformational changes of the pore lining helices. Each helix was described as two ideal right cylinders joined at the center by a common point [see Figs. 1(a) and 1(b)]. Therefore, the orientation of each helix is completely described by a set of three points: p1—the top of the upper cylinder, p2—the point joining both cylinders, and p3—the end of the lower cylinder. Throughout the text, we refer to the p3 position as the "tail position," since this corresponds to the C-terminus of the helix. We used the S6 helices from the Kv1.2 structure (PDB code 2A79) and the M2 helix from KcsA (PDB code 1K4C) as our starting points to define p1, p2, and p3. First, each channel was aligned with the z-axis. These x-ray structures have fourfold symmetry, so the positions of all four inner helices can be generated from one helix by carrying out rotations about the z-axis. Each point describing the cylinders roughly corresponds to the center of mass of four C_α atoms at the top (p1), middle (p2), or bottom (p3) of the helix, and the location of the middle point was defined by the first proline in the PVP motif for Kv1.2 or by the glycine hinge, G99, for KcsA. Each cylinder was given a uniform radius of 3.75 Å, which approximates the spatial extent of the helix. We kept the upper two points fixed and allowed the helix tail (p3) to move through all possible configurations. Movement of the lower cylinder can be described by two angles: the kink angle, which is the angle formed between the axis of the upper cylinder (p2-p1) and the lower cylinder (p3-p2), and the swivel angle, which indicates the direction that the lower cylinder moves with respect to a fixed point on the upper cylinder. When the helix tail kinks in the direction toward the C_α atom of the hinge residue, either P405 or G99, the swivel angle is zero. If the helix kinks away from the C_α atom, the swivel angle is 180°. We discretely changed the swivel angle from 0 to 2π, and for each swivel value, the kink angle was swept from 0 to $\pi/2$. This displacement was then symmetrically applied to the other three helices. For each configuration, we determined if a clash occurred between any cylinders, and if not, the pore diameter was calculated using the distance between opposite helix tails (p3). We then projected the entire set of tail positions onto a plane perpendicular to the axis of the upper cylinder in order to visualize which movements of the lower cylinder result in plausible pore conformations.

B. Molecular dynamics simulations

All atomistic simulations were carried out using NAMD (Ref. 27) with the CHARMM27 parameter set[28,29] and VMD (Ref. 30) for visualization. The four S6 helices (residues I385-H418) from the Kv1.2 crystal structure (PDB code 2A79) were extracted from the rest of the protein and the helix termini were modified with N- or C-terminal patches. VMD was used to solvate the system using the TIP3P water molecule resulting in a final system size of $64\times64\times72$ Å^3 and 27 000 atoms. Four chloride ions were added for electroneutrality. Periodic boundary conditions were applied in all three directions. Point mutations (P405A, L404A, A403V, L404I, and A403G) were made with NAMD psfgen module. First, conjugate gradient minimization was performed followed by equilibration for 60 ps with the NPT ensemble to remove water defects. The Langevin piston method was used to control pressure ($P=1$ atm) and temperature was increased every 50 steps by 1 K until it reached 300 K using Langevin dynamics with a damping coefficient 10 ps^{-1} as a thermostat. Next, the system was further equilibrated for 1 ns using the NVT ensemble. After equilibration, a 50 ns production run was carried out for each structure [wild-type (WT) plus five mutants] for a total of 0.30 μs of simulation. The time step was set to 2 fs and trajectories were saved every 50 steps for analysis. All hydrogen atom-heavy atom bond lengths were constrained using the SHAKE algorithm.[31] A cutoff of 10 Å was used for the van der Waals interactions and the particle mesh Ewald summation was employed. The backbone atoms of residues I385-G398 were restrained with a harmonic constant $k_1=2.0$ kcal/(mol Å^2). We also restrained the O–HN distance and the O–N distance between N414 and H418 at the C-terminus using a force constant $k_2=2.0$ kcal/(mol Å^2). These distances were set to 2 and 3 Å, respectively.

C. Intrinsic motions of the inner helix

We wanted to quantitatively investigate the mechanics of helix bending based on our equilibrium MD simulations. To do this we used a coarse grained model of the helix based on a comparison to an elastic rod.[32] The helix configuration is described by local curvatures and twists along the backbone rather than all of the degrees of freedom of all of the atoms in the helix. This is calculated by erecting a body-fixed coordinate frame $(\vec{e}_1,\vec{e}_2,\vec{e}_3)$ along the entire length of the helix. Each local frame is defined by four consecutive residues and each group is called a *slice*. We defined the slices for each S6 helix as follows:

385 IGGK IVGS LCAI AGVL TIAL PVPV IVSN FNYF YH 418,
1 2 3 4 5 6 7 8

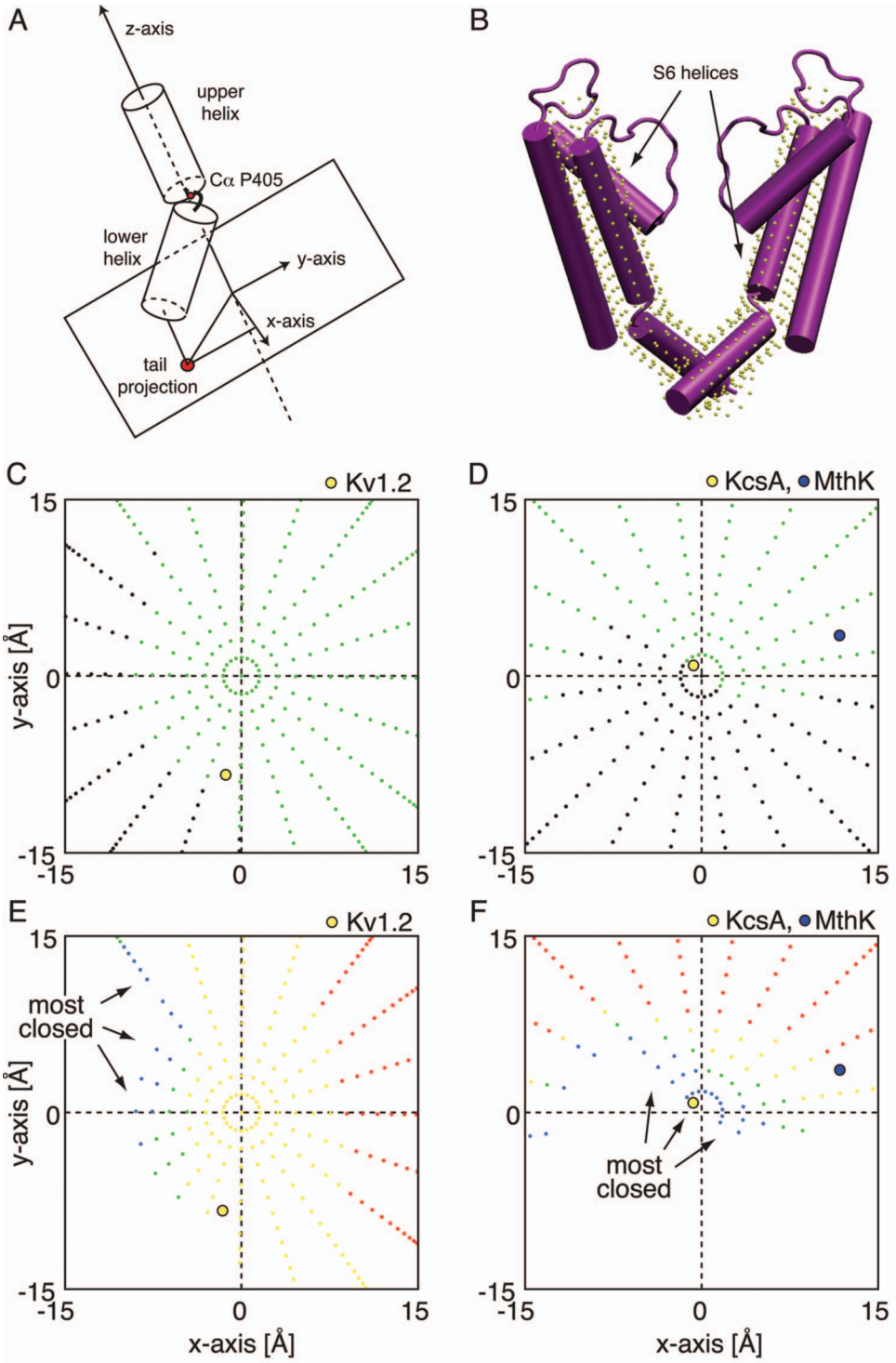

FIG. 1. (Color) (a) A diagram of the hinged-rod model. Each helix is described as two ideal right cylinders joined at the center of a common point. The orientation of each helix is completely described by a set of three points: p1 at the top of the upper helix, p2 at the point joining both cylinders, and p3 at the end of the lower helix. The C_α atom of the hinge residue is either P405, the first proline in the PVP motif, or G99, the glycine hinge in KcsA. The helix tail position described by p3, or points near p3, is projected into a plane perpendicular to the upper helix. This plane is determined by the vector p1-p2, and the *x*-axis of the plane is aligned with C_α atom of the hinge residue. Analysis of the fully atomistic simulations is carried out in the same manner. (b) Two adjacent subunits from the Kv1.2 structure (purple) are shown. The corresponding hinged-rod model is superposed on the inner helices (yellow spheres). The spheres fall on the surface of a cylinder of radius 3.75 Å, and p2 coincides with the break in the S6 helices. (c) The *x*-*y* projection of the tail position (p3) in Kv1.2. Green dots denote sterically permissible positions and black dots denote positions that are not possible. The yellow circle shows the *x*-*y* projection of the original Kv1.2 x-ray structure. (d) Same as in panel (c) for the KcsA channel. The positions of the MthK and KcsA x-ray structures are shown. (e) The degree of pore opening for Kv1.2 corresponding to panel (c). The pore radius for the hinged-rod model is denoted by the color of the dot: blue $-<3.75$ Å, green -3.75 to 4.75 Å, yellow -4.75 to 5.75 Å, and red $->5.75$ Å. (f) Same as in panel (e) for the KcsA channel.

where each slice number is indicated below the grouping. The positions of the backbone α-carbons for the first three residues in the slice define a triangle used to construct the local frame. The unit tangent vector, $\vec{e}_3$, is defined by the centroids of two neighboring slices; thus, $\vec{e}_3$ points along the helix. Next, we defined a vector $\vec{e}'$ using the centroid of the triangle and the midpoint of the edge between atoms 1 and 3 in the triangle. $\vec{e}_3 \times \vec{e}'$ is defined as $\vec{e}_2$. Then, it follows that $\vec{e}_1 = \vec{e}_2 \times \vec{e}_3$. This procedure was performed for all slices in the helix at all time points of the trajectory. Using the local coordinate frame, we extracted the intrinsic fluctuations inherent to the movement of the helix. These motions are described by three torsion angles, ω_1, ω_2, and ω_3, which relate the local coordinate frames between adjacent slices by[32]

$$\vec{e}_i(s) = \sum_j R_{ij}(s,s')\vec{e}_j(s'), \tag{1}$$

where s and s' denote different points along the arc and R_{ij} is the rotation matrix between adjacent coordinate frames. R can be rewritten as

$$R = \exp(-\Omega \Delta s), \tag{2}$$

where $\Omega_{ij} = \Sigma_k \epsilon_{ijk}\omega_k$, ϵ_{ijk} is the antisymmetric Levi–Civita tensor, and Δs is the average distance between slices. Note that the rate of change in the coordinate frame is given by the Frenet equations,

$$\frac{\partial \vec{e}_i}{\partial s} = -\sum_{j,k} \epsilon_{ijk}\vec{e}_j\omega_k. \tag{3}$$

Equation (3) shows that the dimension of ω is [1/length], and this was also explicitly shown in Eq. (2). ω_1 and ω_2 correspond to two bending modes of the helix, while ω_3 corresponds to one twist mode. The bending modes are related to the kinking of the helix and the twist mode is related to unwinding and overwinding of the helix along its axis. For an ideal α-helix $\omega_{01} = \omega_{02} = 0$, and $\omega_{03} = -0.1$, where ω_{01}, ω_{02}, and ω_{03} are intrinsic torsion angles (see Ref. 32 for more details). Note that there are different methods to describe the internal configuration of helices. For example, Kneller and Calligari presented a simple method, *ScrewFit*, for the characterization of protein secondary structure, which is based on quaternion superposition fits of consecutive peptide planes.[33]

III. RESULTS AND DISCUSSION

A. Orientation and hinge placement affect pore opening

While many researchers believe that glycine and proline residues provide a hinge point about which the lower portion of the inner helix can pivot, there is much less speculation upon the extent of motion of the upper portion of S6. Yellen and co-workers[19] use their functional data to support the notion that the upper portion of S6 remains relatively rigid during gating, which is in accord with MD simulations and NMA analysis showing that the region of the pore near the selectivity filter undergoes the smallest amplitude motions.[34–36] Additionally, superposition of MthK onto KcsA reveals that the inner helices are perfectly aligned in the region above the glycine hinge. However, the N-terminal ends of S6 from Kv1.2 show a slightly different orientation and the P405 hinge residue is significantly farther along the helix than the G99 residue in KcsA. Additionally, the hinge region in Kv1.2 is several angstroms farther away from the central axis than in either MthK or KcsA. To explore the impact that these differences have on the mechanism of channel opening, we constructed a very simple, but general, hinged-rod model. The upper and lower portions of the inner helix were treated as rigid cylinders joined at the center by a hinge point. The location of the hinge point for the model based on Kv1.2 was centered on the first proline in the PVP motif, while the hinge for the KcsA model was centered on G99. We then systematically moved the C-terminal end of the inner helices through many different positions and recorded those that did not result in a steric clash with the other three helices. While this simple approach ignores the role that side chains can play in controlling the degree of pore closure,[5] it completely explores the role between how and where a helix bends.

We can see from the maps in Figs. 1(c) and 1(d) that the opening and closing of KcsA is much more restrictive than Kv1.2. The angle of allowed openings (green dots) is much smaller for KcsA than it is for Kv1.2. When the Kv1.2 inner helix is straight, it can move in any direction to open, while KcsA must move within a swivel angle of $-10°$ to $+125°$ to open. Interestingly, the corresponding kink and swivel angles of the MthK inner helix fall in the allowed region based on the KcsA analysis (blue circle). Also, in the KcsA model, MthK bends toward the C_α atom of the hinge residue, while in Kv1.2 x-ray structure the helix bends 90° away from the C_α atom of P405. This may be a general property of glycine hinges versus proline hinges.

Next, we plotted the degree of pore closure in a similar manner to the graphs in panels C and D. In Figs. 1(e) and 1(f) the allowed configurations were assigned a color code based on how closed or open the channel was. This was calculated by determining the distance of closest approach of the inner helices to the pore axis. The closest configurations are denoted by blue dots, next most closed are green, moderately open are yellow, and then the most open configurations are red. We see in panel E that Kv1.2 is moderately open and the most closed states involve moving the helix tail into quadrant II, which requires a bending away from the C_α atom of P405. Thus, a straight helix may not effectively close the channel unless straightening the helix involves moving bulky residues into the permeation pathway. On the contrary, the inner helices of KcsA are very straight and they effectively close the channel (Fig. 1(f)). To explore this aspect more fully, we introduced more flexibility into the model by allowing the middle point (p2) to move up to 5 Å from its initial position during the calculation of the clash free maps. This changed some aspects of the maps; however, the degree of pore closure was not greatly affected for either the KcsA or Kv1.2 analysis.

B. Helix-tail distributions from MD simulations

Point mutations in the inner helix affect the gating of channels,[37,38] but it is not known if these perturbations result

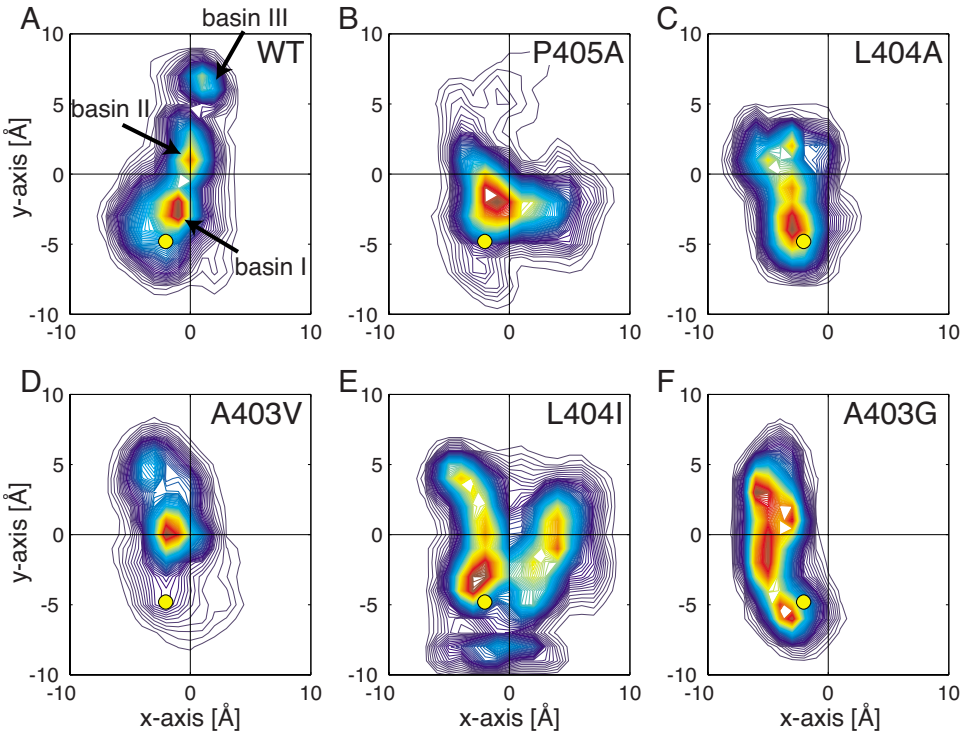

FIG. 2. (Color online) The *x*-*y* projection of the helix tail positions of WT and five mutants using MD simulations. The circle corresponds to the *x*-*y* projection of S6 helix in the original Kv1.2 x-ray structure. The points in the trajectory are represented by contour plots, where dark interior regions indicate high probability regions and dark border areas represent low probability regions. (a) WT simulations show two spatially distinct basins that are highly populated and a third basin corresponding to helix configurations that are less probable. Basin I is very close to the starting structure, basin II corresponds to a nearly straight helix, and basin III is highly bent. (b) The P405A mutation removes the bistability of the helix and there is only one large basin. All of the other PVP containing helices show multiple distinct basins. [(c) and (d)] L404A shows a strong basin near the Kv1.2 open structure (circle), while A403V shows a very low probability of the helix tail being near the initial starting structure. (e) The L404I mutation shows large excursions throughout the entire plane of the helix and two large basins separated by 10 Å. (f) A403G is characterized by one long basin running between quadrants II and III. This helix spends very little time at positive *x*-axis values, which indicates its tendency to bend away from the P405 position.

from a global disturbance to the channel packing or if they can be explained by local changes in the biophysical properties of the inner helix. To examine the impact that point mutations have on the mechanics of individual helices, we employed fully atomistic MD simulations on the inner helix of the Kv1.2 channel. We extracted 34 residues (I385-H418) of the S6 helix from Kv1.2 to use as an initial configuration for all simulations. The local environment of the inner helix is complex. It is largely surrounded by protein at its N-terminal end, while it is largely solvated by water, and probably lipid, at the C-terminal end. We chose to carry out these simulations in water and we restrained the C_α positions of the upper helix (the N-terminus) to mimic the effect of tight packing around the selectivity filter and other TM helices. We know from the KcsA and KirBac structures that the inner helices are tightly packed in the closed states. Therefore, we considered two sets of simulations: one in which the helix was simulated by itself and another in which all four symmetric copies were simulated simultaneously.

We investigated the properties of the wild-type helix and five point mutants in and around the PVP motif. Our initial analysis of the S6 helix from Kv1.2 revealed that the dihedral angles of A403 and L404, the residues directly preceding PVP, are far from ideal. A403 takes on a ψ value of +50°, L404 has a ϕ value of −140°, while typical α-helical values are −50° and −60°, respectively. We surmised that these angles may be important in hinge bending and that gating may involve the pre-proline residues moving between distorted and typical values. Interestingly, the most recent Kv1.2/2.1 chimera structure (PDB code 2R9R),[39] which is higher resolution than 2A79, does not exhibit these atypical dihedral angles for these pre-proline residues, and when we simulated the inner helices from 2A79, the dihedral angles of A403 and L404 relaxed to the values found in the Kv1.2/2.1 chimera structure (data not shown). Nonetheless, the alanine and leucine residues are highly conserved[35] and they are clearly important to channel gating. Thus, we chose to investigate the following mutations, which have all been experimentally tested: A403G (A471G), A403V (A471V), L404A (L472A), L404I (L472I), and P405A (P473A), Shaker numbers in parenthesis. Specifically, the A403V mutation abolishes channel expression in Shaker,[38] and the corresponding mutation in the KCNQ1 channel, A341V, is implicated in long QT syndrome, a cardiac arrhythmia.[40] L404A reduces Shaker channel function[38] and the corresponding mutation in KCNQ1 reduces channel function as well.[41]

We started by investigating the equilibrium motions of the four inner helices. In order to simplify the complexity, we tracked the tail of the C-terminus over the entire 50 ns of the simulation, and in Fig. 2 we projected the tail position into a plane perpendicular to the axis of the upper portion of the helix, as in Fig. 1. The points in the trajectory are represented by contour plots, where dark interior regions indicate the most probable regions of finding the helix tail and dark bor-

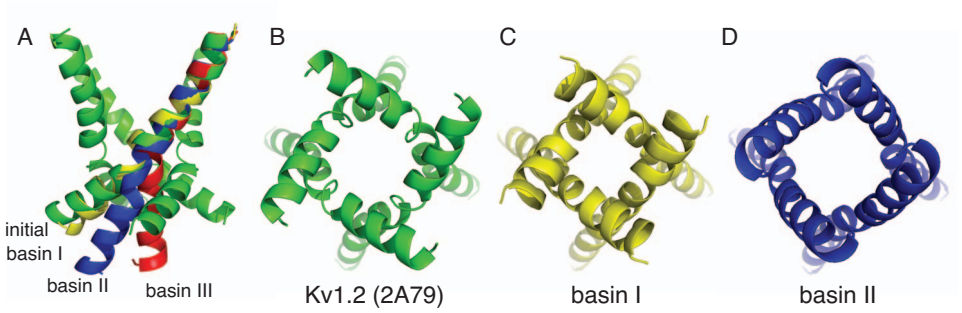

FIG. 3. (Color) Representative conformations from each of the basins in Fig. 2(a). (a) Three conformations are aligned to the original Kv1.2 x-ray structure (green). The conformation from basin I is yellow, that from basin II is blue, and the conformation from basin III is red. These configurations were used to create panels (b)–(d). Each helix was rotated about the z-axis to create a symmetric tetramer of inner helices. (b) Conformation from the original x-ray structure (bottom view). (c) Conformation from basin I (bottom view). This configuration is very similar to the initial x-ray structure. (d) Conformations from basin II (bottom view). While this helix is much straighter, it does not close the pore domain as is seen in KcsA.

der areas represent regions of low probability. When the helix tail is at the origin the helix is completely straight and when the helix tail falls along the positive x-axis, the helix is bending toward the C_α atom of P405. The circle in each panel indicates the x-y projection of the S6 helix in the original crystal structure. The simulation corresponds to four helices, while the data in each panel is represented as if it comes from one helix. To do this, we superposed the trajectories from all three helices onto one contour plot by carrying out the appropriate rotations in the x-y plane.

We see from the helix-tail distributions in Fig. 2 that the natural motions of the wild-type S6 helix are distinct from each of the mutant helices. This suggests that the impact that point mutations have on channel function may in fact be understood through their influence on the bending properties of the inner helix. In each case, the patterns are highly anisotropic unlike the radially symmetric patterns we would expect from helices behaving like elastic rods. This result is in contrast with the findings from Choe and Sun[32] in which they showed that helices of varying sequences typically exhibit isotropic bending motions centered on a straight helix. The difference in these two studies is certainly related to the presence of proline residues, which were not investigated by Choe and Sun. Interestingly, WT simulations show two spatially distinct basins, one near the origin (basin II) and the other in quadrant III very close to the initial Kv1.2 structure (basin I), which corresponds to a bend 90° away from the C_α atom of P405. The presence of two highly probable configurations is exactly what one would expect of a helix that has to switch between two states: closed and open. There is a less well populated third basin (basin III), which corresponds to a highly kinked helix nearly 180° away from basin I. Representative structures from each of these basins are superposed on the original Kv1.2 x-ray structure (green) in Fig. 3(a), basin I (yellow), basin II (blue), and basin III (red). Examining these pores from the cytoplasm reveals that all three structures are relatively open, even basin II (panel D) in which the helix is straight. This result is consistent with our result from the hinged-rod model, where we showed that a straight helix does not effectively close the channel. However, from Fig. 1(e) we also see that there are configurations in quadrant I in which the channel is closed and the positions of helices in basin II are closer to that position than the starting configuration or basin I.

We estimated the energy of the representative helices from each basin by using the elastic rod model in conjunction with the results from our MD simulations. First, from the torsion angle probability distributions, like those shown in Figs. 4 and 5, we fit each distribution to a quadratic function. This gave us the intrinsic torsion angles, ω_{01}, ω_{02}, and ω_{03}, and corresponding bending moduli at each slice. From these values, we estimated the total elastic energy of each configuration in Fig. 3 using linear elasticity theory (see Choe and Sun[32] for more details on these calculations). The calculated elastic energy was 9.6, 13.7, and 15.3 k_BT for the structures from basins I, II, and III, respectively. The conformation in basin I has the lowest energy. This is certainly related to the fact that this is the most highly populated basin [see Fig. 2(a)]. Additionally, the energy required to stabilize a helix in basin II or III relative to basin I is 4–6 k_BT, which is consistent with gating being an activated process that rarely happens spontaneously. Finally, these energy values must be interpreted with care since they are calculated assuming that the helices obey linear elasticity, which is clearly not the case for some basins, which show nonlinear elastic behavior (see Figs. 4 and 5). Thus, the elastic energy cannot be represented by a simple quadratic function of ω, and more quantitative analysis is needed to obtain better estimates of the true energy differences.

Interestingly, replacing P405 with an alanine abolishes the two state behavior observed for the WT helix [Fig. 2(b)]. Instead, we see one dominant basin centered near the origin corresponding to an intermediate configuration between the starting Kv1.2 structure and a straight helix. Alanine has the ability to hydrogen bond with T401, which stabilizes the segment in a more straight α-helical configuration. Thus, it would seem that the bistable nature of the helix, and therefore opening and closing, is dependent on the presence of the first proline. This is consistent with previous experiments, which showed that the PVP motif plays an essential role in gating, and there appears to be an absolute requirement for the presence of the first proline.[18] Several groups claimed that the proline residues and the residue between them form a flexible "hinge" region, which may serve as a pivot point during channel opening and closing as suggested previously.[18,42,43] L404A shows a strong basin near the Kv1.2 open structure (circle), which is interesting since this

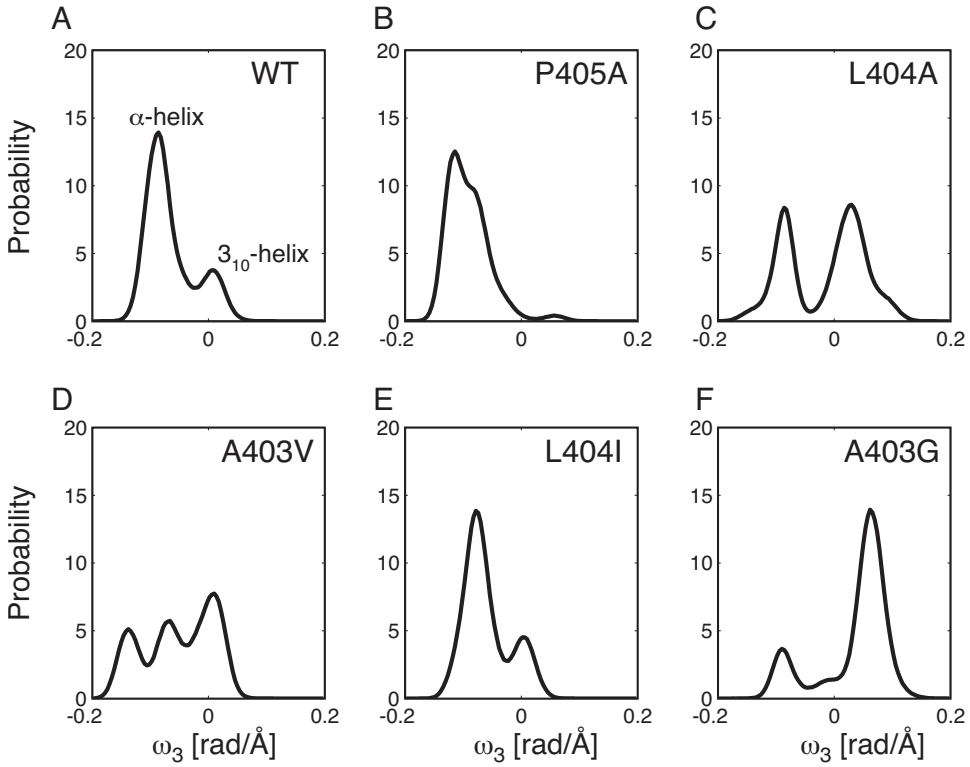

FIG. 4. ω_3 torsion angle probability distributions near the PVP motif for WT and five mutants. ω_3 reflects the amount of twisting about the long axis of the helix. (a) The WT helix exhibits two strong peaks corresponding to the local adoption of an α-helix, larger left peak centered on -0.1, and a 3_{10}-helix, right peak centered on 0. (b) Mutating the first proline, P405, to an alanine completely removes the ability of the helix to locally adopt a 3_{10}-helix leaving a single broad distribution corresponding to α-helical configurations. [(c)–(f)] All mutations prior to the PVP motif failed to remove the multimodal property of the helix; however, these mutations severely altered the shape, position, and relative heights of each peak. Both L404A (c) and A403G (f) show strong peaks with positive ω_3 values, which indicates that these helices are unwinding. L404I (e) has a distribution nearly identical to WT; however, A403V (d) adopts a 3_{10}-helix, to a lesser extent an α-helix, and finally it adopts a torsional state that is intermediate to both of these.

mutation reduces channel function.[38] This reduction could be related to the fact that there is only one other significantly populated basin, which is functionally merged with the first basin [Fig. 2(c)]. In fact, all of the helices are characterized by multiple conformational basins except for P405A. The A403V mutant exhibits one dominant basin in which the helix is straight, while a second, less probable basin is present in quadrant II (panel D). There is a relatively low probability for the helix tail to occupy the initial position of the open Kv1.2 structure, which may be related to the nonfunctional nature of mutations at this position.[38] The L404I mutant shows two highly populated basins that are separated by 10 Å (panel E). The basin on the left encompasses configurations similar to the starting open Kv1.2 structure, but the basin extends in the y direction into quadrant II along a long valley. The second basin is located in quadrant IV and it is also highly populated. The presence of a long narrow valley of probable conformations connecting regions in quadrants III and II is also seen in the A403G mutant (panel F); however, A403G rarely bends the helix toward the C_α atom of P405.

It is interesting to speculate that basin I represents the open state of the channel and that basin II represents a configuration toward the closed state. We have not simulated the pulling forces that the S4-S5 linker exerts on the helix. Presumably any systematic force would bias the exact location of these basins in the x-y plane, possibly pulling basin II into a more closed configuration and basin I closer to the open state. The contour maps in Fig. 2 are superpositions of all four helices from each 50 ns simulation. While our simulations are five to ten times longer than previous studies of S6 helix motions,[21,43,44] it is important to note that the solo distributions from each individual helix do not always match the compiled distribution. Therefore, while we hope that the compiled data set is more representative of the true equilibrium helix-tail distributions of four inner helices, we are cautious to make this claim.

C. Local motions of the PVP region indicate it is primed to be bistable

One of our goals is to understand the role of proline in the gating mechanism. Proline residues not only contribute to a disruption of secondary structure by allowing helix bending, but they also increase torsional flexibility. Our previous analysis of the helix-tail distributions gave us information on the global changes of the helix, but it did not give detailed information as to how the hinge position is affecting these global changes. We used the results from the MD simulations to calculate the local bending and torsion values of the helix near the PVP motif to answer these questions.

An α-helix has a nonzero intrinsic torsion about its long axis due to its natural helicity. As a helix undergoes fluctuations and structural transitions, this value will change, and therefore, it takes on a distribution of values. The torsion

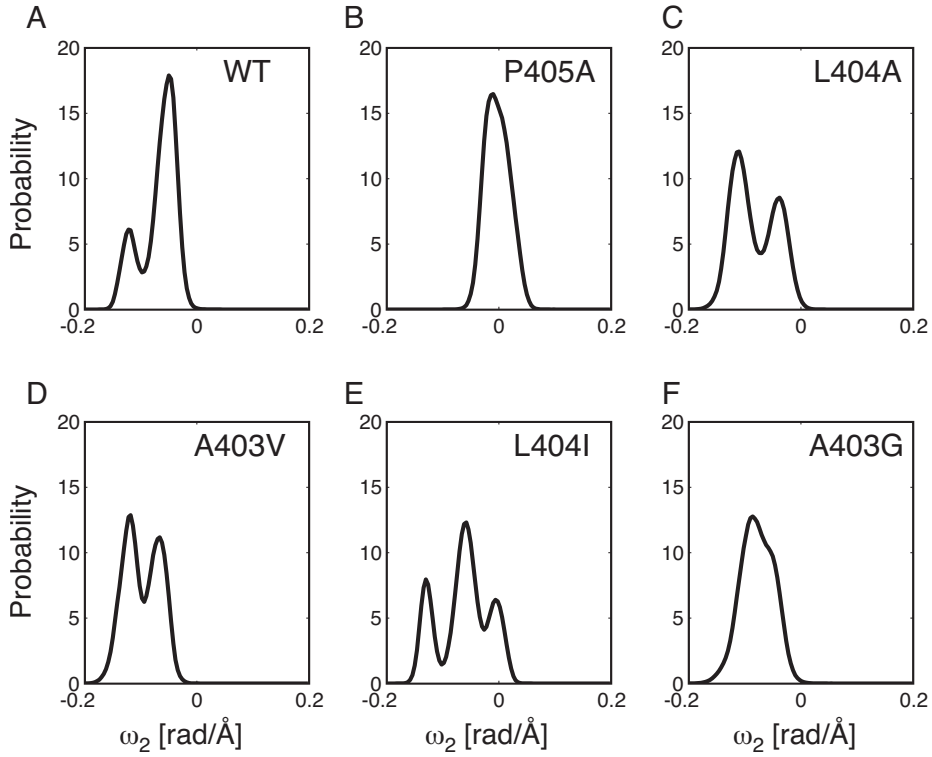

FIG. 5. ω_2 torsion angle probability distributions near the PVP motif for WT and five mutants. ω_2 indicates the degree of local bending about the long axis of the helix. (a) The WT helix exhibits two prominent peaks indicating the local adoption of two kink values. Neither value is centered on zero indicating this region is always kinked. The small peak on the left corresponds to the small peak in Fig. 4(a) of helices that have locally adopted a 3_{10} state. (b) P405A completely removes the bimodal nature of the helix near the PVP region and the helix locally adopts a straight conformation centered on zero. [(c)–(e)] Pre-P405 mutations critically affect the distribution of local bending but each helix retains its ability to adopt multiple distinct bending conformations. (f) Introducing a glycine residue at position 403 also removes the bimodal character of the helix. Instead, the PVP region is characterized by a constant torsion value around −0.1, but the distribution is very broad indicating that this helix is flexible.

angle ω_3 measures the twist along the long axis from one slice of four residues to the next slice. With this definition, ω_3 is −0.1 rad/Å for an ideal α-helix. Figure 4 shows the distributions of ω_3 calculated between the fourth and fifth slices compiled over the entire time course of each simulation. Although the P405 is located at the sixth slice, ω_3 is affected by the movement of the PVP motif due to the definition of $\vec{e}_3$. The WT simulations exhibit two well defined peaks, one centered on −0.1, which corresponds to an ideal α-helix, and another peak centered on $\omega_3=0$, which corresponds to the local adoption of a 3_{10}-helix. Bimodal distributions are exactly what we would expect of a system that is designed to exist in two distinct states, open and closed. Similar simulations of polyalanine and random sequence α-helices only observed a normally distributed set of values centered on −0.1;[32] however, the Kv1.2 sequence appears to be able to switch between the two most frequently observed helical conformations. Nonetheless, P405A shows only one major peak corresponding to an ideal α-helix. This is to be expected since the alanine has the ability to hydrogen bond to the $(i-4)$th residue and lock the helix into a low energy α-helical conformation making it difficult to switch between different axial torsion states. The other mutants severely alter the torsional properties of the helix [Figs. 4(c)–4(f)], but all of them show multimodal distributions. The bimodal behavior of the WT helix is clearly dependent on the presence of a proline at position 405, but it may also depend on the particular sequence of the surrounding residues, specifically P407. Further analysis is required to more fully explore this possibility.

L404I has a nearly identical distribution to WT [Fig. 4(e)]. L404A has two strong peaks also of nearly equal height, but the peak corresponding to the 3_{10}-helix is right shifted, which means that the helix is slightly unwinding. A403V shows three peaks and the largest one is located near $\omega_3=0$. In aqueous solution, valine is known to have a high propensity to form β-sheets and a low propensity to form α-helices, which may be related to this behavior. A403G introduces a glycine residue before the first proline in the PVP motif, and it clearly perturbs the helix properties. As noted previously glycine does not have a side chain, and it can adopt dihedral angles in all four quadrants of the Ramachandran plot. In other words, it is ideally suited to provide flexibility. The most probable torsion angles are positive, indicating that the helix is unwinding. This result is in excellent agreement with similar simulations carried out on a polyglycine helix.[32]

Next we computed the torsions corresponding to local bending and we present ω_2 calculated between slices 4 and 5 in Fig. 5. The wild-type helix shows two well defined peaks just as it did for ω_3, again suggesting that this particular helix is ideally suited to adopt two stable conformations. Interestingly, the larger peak is not centered on zero, which means that this section of the helix is not straight, but slightly

kinked. We also asked if the smaller peak, which takes on larger bending values, is correlated with the smaller set of configurations that adopt a local 3_{10}-helix in Fig. 4(a); indeed these larger local kink values are all related to a local unwinding of the helix. Mutation of P405 to alanine completely removes the second peak and centers the distribution on zero, corresponding to a locally straight helix [Fig. 5(b)]. This is the only simulation that shows this behavior and it is in excellent agreement with what we see for P405A ω_3 values and the helix-tail distributions in Fig. 2(b). In panel C, L404A shows a distribution similar to WT, but the relative heights have changed, and the peak corresponding to a larger bend has a higher probability. A similar pattern is seen in panel D with A403V, but both peaks have nearly equal height. The most interesting distribution is L404I, panel E, which has three primary peaks with one centered on zero. The final glycine mutation also has one dominant peak like P405A, but the helix is locally kinked and never straight [Fig. 5(f)]. Additionally, the width of the distribution is quite wide, which indicates that the helix has increased local flexibility as seen previously for polyglycine helices.[32] In Fig. 2(f) the helix tail never adopts a straight conformation and this may be related to the inability of the helix near A403G to straighten.

We explored the impact that our choice of residue grouping had on our results. The purpose of this bracketing is to group adjacent residues along the helix into blocks to obtain a simplified description of the helix. It is natural to pick groups of four for an α-helix since there is typically a hydrogen bond between the ith residue and $(i$-4)th residue. However, which four residues get grouped together will affect the subsequent calculations of the torsion angles. Therefore, we made two different systems by shifting the grouping one residue forward and one residue backward from our original grouping shown in Sec. II:

385 IGG KIVG SLCA IAGV LTIA LPVP VIVS NFNY FYH 418,
(1) (2) (3) (4) (5) (6) (7)

385 I GGKI VGSL CAIA GVLT IALP VPVI VSNF NYFY H 418.
(1) (2) (3) (4) (5) (6) (7) (8)

Again, the torsion angle distributions near the PVP motif showed two peaks for the WT calculations but only one peak for the P405A mutant, showing that our results are robust with respect to the choice of coordinate frame.

D. Helix bending is correlated with the local twisting near the PVP motif

We wanted to know if there is a connection between whether the PVP region has locally adopted a 3_{10}- or an α-helix and whether the helix tail is straight or bent. To do this, we classified points in the wild-type MD simulation as being in a 3_{10} or an α-helical state based on our results in Fig. 4(a). We recomputed the helix-tail distributions from Fig. 2(a) to give us Fig. 6(a) for ω_3 near -0.1 and Fig. 6(b) for ω_3 near 0. Clearly, when the PVP region adopts a 3_{10}-helix the helix is globally straight, and when the segment locally adopts an α-helix, the helix has a much higher probability to be in a kinked or bent state. To further quantify the maps in panels A and B, in Fig. 6(c) we plotted the radial distribution function of the helix-tail projection using the following equation:

$$g_n = \frac{h_n}{\pi(2\cdot(n-1)+1)\Delta r^2 \rho}, \tag{4}$$

where $n=1\cdots$ total number of bins, $\rho=N$ (total configurations)$/A$ (total area), and h_n is the number of configurations in each bin. The data in panel A are shown as a solid curve and the data from panel B are a dashed curve. When the PVP region has unwound into a 3_{10}-helix, the helix adopts a globally straight conformation that is 7.5 times more likely than bent conformations. Around 2.5 Å the density of configurations has fallen below the uniform value indicating that, globally, the helix does not deviate from straight when the PVP region is in the 3_{10} state. This is interesting since in the last section we showed that the local unwinding of the helix locally produces large ω_2 values. From the inset, we see that while these helices are locally bent near the PVP region, this produces a global helix that is quite straight from N- to C-terminus [Fig. 6(c)]. When the PVP region adopts a local α-helical ω_3 value, the distribution of global kink values becomes much more broad producing tail movements as large as 7.5–8 Å with a peak near 3 Å. These results suggest the distinct possibility that helix straightening and possibly pore closure is accompanied by an α-helix to a 3_{10}-helix transition near the PVP region.

All of the simulations presented thus far involved four helices extracted from the inner pore of Kv1.2, but we wanted to know if the dynamics of a single inner helix is different from that of four helices simulated simultaneously. To examine this question, we removed three of the helices from the initial starting configuration and carried out an additional 50 ns of simulation. We compared the distribution of kink angles for a single helix with the distribution from four S6 helices and as we saw in Figs. 2(a) and 5(a) that four wild-type helices exist in two well-defined kink states, but a single wild-type helix does not exhibit two peaks (data not shown). Instead, the solo helix shows a broad continuum of kink angles centered on 20°, but extending from 0° to 50°. So while the two state behavior observed earlier is critical to the bistable character of a channel, which must be open or closed, it appears that this is a multibody property that is

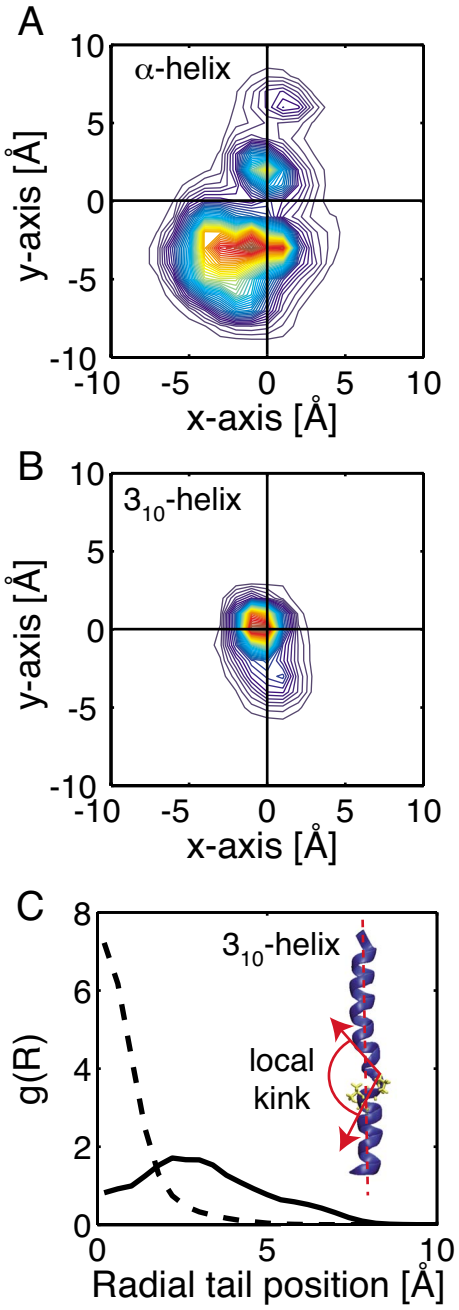

FIG. 6. (Color online) Analysis of the mechanism of helix bending. (a) and (b) Contour map of the helix tail distribution for the subset of configurations corresponding to an α-helical (a) or a 3_{10} ω_3 value at the PVP region. From panel (a) we see that basin I in Fig. 2(a) is largely made up of helices in the α-helical conformation, while basin II is dominated by configurations that are in the 3_{10} state. (c) Radial distribution of the helix tail positions in panel (a), α-helix (solid curve), and panel (b), 3_{10}-helix (dashed curve). The radius R measures the position of the helix tail position, $R=\sqrt{x_{\text{tail}}^2+y_{\text{tail}}^2}$. The density of straight helix configurations is 7.5 times higher than the average value when the PVP region has locally adopted a 3_{10}-helical state. Meanwhile, the distribution is much broader when the helix adopted an α-helical state, and it can exhibit a much higher degree of bending. A side view of the helix from basin II is provided to show that while the helix is globally straight (falls along the dashed line), the region near the PVP motif (residues in licorice) is highly kinked (solid lines). The helix is the same basin II helix shown in Fig. 3. The average density is crucial to calculating the radial distribution function. For the α-helical conformations we estimated the total accessible area based on the contours in panel (a) to be 150 Å^2. Similarly, we estimated the area to be 55 Å^2 for the 3_{10} conformations.

only seen in the presence of more than one helix. That said, the two state behavior is still dependent on the channel sequence, since the P405A mutant only exhibits one stable configuration even in the presence of four helices [see Figs. 2(b), 4(b), and 5(b)]. This same behavior was also reported by Bright *et al.*[44] in which they showed that S6 helices adopt two dominant kink angles when simulated in the entire pore domain, S5-S6, and only one dominant kink angle when simulated alone. Also, our distribution of kink angles for a single S6 helix simulated in water is quantitatively similar to the distribution calculated for the Shaker S6 helix in an octane slab.[42] It has been previously observed that the elastic properties of helices are insensitive to the surrounding environment,[32] and this observation together with the results carried out in an octane slab suggest that the bimodal nature of the kink angle and ω_3 torsional angle may be intrinsic properties of four juxtaposed S6 helices. Thus, while our simulations are carried out on a reduced system, these observations may hold true for the full channel system.

IV. CONCLUSION

We showed that the natural motions of the inner helix from Kv channels are highly anisotropic, as shown before,[21,42–44] and that single point mutations can dramatically affect the range and motion of the helix tail. We were able to show that the wild-type Kv1.2 inner helix adopts multiple, spatially distinct conformations and that mutating the first proline in the conserved PVP motif abolishes this multimodal behavior resulting in a single broad basin. It is likely that the bi- or multistability of the wild-type helix is critical to its role as a gate keeper that must switch between open and closed states. Most interestingly, we showed that the local configurational state near the PVP region is highly correlated with the position of the C-terminal end of the helix over 10 Å away. Specifically, we showed that when the helix locally adopts a 3_{10}-helix at the PVP region, the helix is globally straight, but that when the region is locally α-helical the entire helix is much more likely to adopt a bent configuration similar to the Kv1.2 x-ray structure. We believe that this is an important result that could lend insight into the mechanical nature of other proline containing helices that must bend to function. However, as suggested by our hinged-rod model, simply straightening the inner helices of Kv1.2 does not tightly close the channel, as has been suggested experimentally.[20] This can be seen in Fig. 1(e) and also in the molecular model in Fig. 3(d), which is constructed from a straight helix, but does not bring about pore closure. The S4-S5 linker and other portions of the channel that were ignored in the present simulations will certainly bias the exact location of the helix tail when forces are applied to S6. A beautiful example of this can be seen by comparing the recent MlotiK1 structure to the Kv1.2 structure.[3,6] The S1-S4 segments of both of these channels are in relatively similar positions but the pore domain of MlotiK1 is closed, while Kv1.2 is open. These differences appear to place a strain on the N-terminus of S5 from MlotiK1 that results in a gentle bend away from the configuration adopted by Kv1.2. Thus, additional forces may bias the configurations in basin II [Fig.

2(a)] to become more closed by moving the tail farther into quadrant II as highlighted by our hinged-rod model [Fig. 1(e)]. However, it may be that configurations such as those in basin III are important for pore closure.

In our present approach, we attempted to probe the intrinsic properties of the inner helices of Kv channels. By design, we omitted portions of the channel with the hope that particular functional properties would still be present in the helices themselves. As discussed above, we think that this is indeed the case, but does everything change when we consider the helices in the full channel embedded in a lipid bilayer? Certainly some things will change; however, our simulations in water are in qualitative agreement with those carried out in an octane slab,[44] and the robust nature of these results supports the notion that the TM helices of Kv channels have intrinsic properties that persist in the full channel. It is interesting to note that recent bilayer simulations of Kv channels show that a large portion of the C-terminus of the S6 helix is exposed to water[45,46] lending credence to our choice to simulate the inner helices in water. With regard to the true gating motions of channels, there is no substitute for actually using the full pore domain to attempt to find the reaction pathway. While our simulations are modestly longer than previous treatments, they are still too short and minimalistic to actually address the true mechanism of channel gating. Therefore, methods designed to specifically handle these long timescale problems are still required.[13,47]

Kv channels contain the highly conserved glycine residue observed in KcsA, G99, but we have not focused on its role in this manuscript. Jiang *et al.*[4] proposed that the PVP motif forms a static kink and that gate opening primarily involves a hingelike motion centered on the glycine, but Elinder *et al.*[48] claimed that the mechanism of opening in prokaryotic (MthK and KvAP) and eukaryotic channels (Shaker and Kv1.2) might differ, reflecting different evolutionary stages. In this scenario a restricted eukaryotic PVP-hinge opening process evolved from a more extensive prokaryotic glycine-hinge opening motion. Our results suggest a dynamic rather than a static role for the PVP motif in gating. In the near future, we hope to apply our methodology to glycine-only containing helices to further explore the differences in these two types of inner helices.

ACKNOWLEDGMENTS

We thank L.Y. Jan, O. Yifrach, L.T. Chong, and J.M. Rosenberg for helpful discussions and M. Lent for both discussions and initial computational work on this project. This work was supported by a National Science Foundation Starter Grant to M.G. (Grant. No. MCB-0722724) and a Medium Resource Allocations Committee Grant from the Pittsburgh Supercomputing Center to S.C. and M.G. (Grant No. MCB070078P). We are also grateful to the Center for Molecular and Materials Simulations at the University of Pittsburgh for valuable computational resources and to R. Christie for his technical expertise.

[1] B. Hille, *Ionic Channels of Excitable Membranes*, 3rd ed. (Sinauer Associates, Sunderland, 2001).
[2] L. Y. Jan and Y. N. Jan, Nature (London) **371**, 119 (1994).
[3] S. B. Long, E. B. Campbell, and R. MacKinnon, Sciences (N.Y.) **309**, 897 (2005).
[4] Y. Jiang, A. Lee, J. Chen, M. Cadene, B. T. Chait, and R. MacKinnon, Nature (London) **417**, 523 (2002).
[5] A. Kuo, J. M. Gulbis, J. F. Antcliff, T. Rahman, E. D. Lowe, J. Zimmer, J. Cuthbertson, F. M. Ashcroft, T. Ezaki, and D. A. Doyle, Science **300**, 1922 (2003).
[6] G. M. Clayton, S. Altieri, L. Heginbotham, V. M. Unger, and J. H. Morais-Cabral, Proc. Natl. Acad. Sci. U.S.A. **105**, 1511 (2008).
[7] D. A. Doyle, J. M. Cabral, R. A. Pfuetzner, A. Kuo, J. M. Gulbis, S. L. Cohen, B. T. Chait, and R. MacKinnon, Science **280**, 69 (1998).
[8] A. Alam and Y. Jiang, Nat. Struct. Mol. Biol. **1**, 30 (2008).
[9] N. Shi, S. Ye, A. Alam, L. Chen, and Y. Jiang, Nature (London) **440**, 570 (2006).
[10] E. Perozo, D. M. Cortes, and L. G. Cuello, Science **285**, 73 (1999).
[11] H. Shimizu, M. Iwamoto, T. Konno, A. Nihei, Y. C. Sasaki, and S. Oiki, Cell **132**, 67 (2008).
[12] G. M. Clayton, W. R. Silverman, L. Heginbotham, and J. H. Morais-Cabral, Cell **119**, 615 (2004).
[13] G. V. Miloshevsky and P. C. Jordan, Structure (London) **15**, 1654 (2007).
[14] C. Domene, D. A. Doyle, and C. Vénien-Bryan, Biophys. J. **89**, L01 (2005).
[15] D. L. Minor, S. J. Masseling, Y. N. Jan, and L. Y. Jan, Cell **96**, 879 (1999).
[16] T. Jin, L. Peng, T. Mirshahi, T. Rohacs, K. W. Chan, R. Sanchez, and D. Logothetis, Mol. Cell **10**, 469 (2002).
[17] Y. Jiang, A. Lee, J. Chen, V. Ruta, M. Cadene, B. T. Chait, and R. MacKinnony, Nature (London) **423**, 33 (2003).
[18] A. J. Labro, A. L. Raes, I. Bellens, N. Ottschytsch, and D. J. Snyders, J. Biol. Chem. **278**, 50724 (2003).
[19] S. M. Webster, D. del Camino, J. P. Dekker, and G. Yellen, Nature (London) **428**, 864 (2004).
[20] D. del Camino, M. Holmgren, Y. Liu, and G. Yellen, Nature (London) **403**, 321 (2000).
[21] J. N. Bright and M. S. P. Sansom, J. Phys. Chem. B **107**, 627 (2003).
[22] E. Emberly, R. Mukhopadhyay, N. Wingreen, and C. Tang, J. Mol. Biol. **327**, 229 (2003).
[23] F. S. Cordes, J. N. Bright, and M. S. P. Sansom, J. Mol. Biol. **323**, 951 (2002).
[24] D. Barlow and J. Thornton, J. Mol. Biol. **201**, 601 (1988).
[25] P. Y. Chou and G. D. Fasman, Biochemistry **13**, 211 (1974).
[26] P. A. Karplus, Protein Sci. **5**, 1406 (1996).
[27] J. C. Phillips, R. Braun, W. Wang, J. Gumbart, E. Tajkhorshid, E. Villa, C. Chipot, R. D. Skeel, L. Kale, and K. Schulten, J. Comput. Chem. **26**, 1781 (2005).
[28] B. R. Brooks, R. E. Bruccoleri, B. D. Olafson, and D. J. States, J. Comput. Chem. **4**, 187 (1983).
[29] A. D. MacKerell, D. Bashford, M. Bellott, R. L. Dunbrack, J. D. Evanseck, M. J. Field, S. Fischer, J. Gao, H. Guo, S. Ha, D. Joseph-McCarthy, L. Kuchnir, K. Kuczera, F. T. K. Lau, C. Mattos, S. Michnick, T. Ngo, D. T. Nguyen, B. Prodhom, W. E. Reiher, B. Roux, M. Schlenkrich, J. C. Smith, R. Stote, J. Straub, M. Watanabe, J. Wiorkiewicz-Kuczera, D. Yin, and M. Karplus, J. Phys. Chem. B **102**, 3586 (1998).
[30] W. Humphrey, A. Dalke, and K. Schulten, J. Mol. Graphics **14**, 33 (1996).
[31] J. P. Ryckaert, G. Ciccotti, and H. J. C. Berendsen, J. Comput. Phys. **23**, 327 (1977).
[32] S. Choe and S. X. Sun, J. Chem. Phys. **122**, 244912 (2005).
[33] G. R. Kneller and P. Calligari, Acta Crystallogr., Sect. D: Biol. Crystallogr. **62**, 302 (2006).
[34] Y. F. Shen, Y. F. Kong, and J. P. Ma, Proc. Natl. Acad. Sci. U.S.A. **99**, 1949 (2002).
[35] I. H. Shrivastava and I. Bahar, Biophys. J. **90**, 3929 (2006).
[36] S. Bernèche and B. Roux, Biophys. J. **78**, 2900 (2000).
[37] D. H. Hackos, T.-H. Chang, and K. J. Swartz, J. Gen. Physiol. **119**, 521 (2002).
[38] O. Yifrach and R. MacKinnon, Cell **111**, 231 (2002).
[39] S. B. Long, X. Tao, E. B. Campbell, and R. MacKinnon, Nature (London) **450**, 376 (2007).
[40] A. Kobori, N. Sarai, W. Shimizu, Y. Nakamura, Y. Murakami, T. Makiyama, S. Ohno, K. Takenaka, T. Ninomiya, Y. Fujiwara, S. Matsuoka, M. Takano, A. Noma, T. Kita, and M. A. Horie, J. Cardiovasc. Electrophysiol. **15**, 190 (2004).
[41] G. Seebohm, N. Strutz-Seebohm, O. N. Ureche, R. Baltaev, A. Lampert,

G. Kornichuk, K. Kamiya, T. V. Wuttke, H. Lerche, M. C. Sanguinetti, and F. Lang, Biophys. J. **90**, 2235 (2006).
[42] D. P. Tieleman, I. H. Schrivastava, M. R. Ulmschneider, and M. S. Sansom, Proteins **44**, 63 (2001).
[43] J. N. Bright, I. H. Schrivastava, F. S. Cordes, and M. S. Sansom, Biopolymers **64**, 303 (2002).
[44] J. N. Bright and M. S. P. Sansom, IEE Proc.: Nanobiotechnol. **151**, 17 (2004).
[45] W. Treptow and M. Tarek, Biophys. J. **90**, L64 (2006).
[46] M. Andér, V. B. Luzhkov, and J. Åqvist, Biophys. J. **94**, 820 (2008).
[47] R. Mashl and E. Jakobsson, Biophys. J. **94**, 4307 (2008).
[48] F. Elinder, J. Niosson, and P. Århem, Physiol. Behav. **92**, 1 (2007).